Proceedings of the ASME 2022
International Additive Manufacturing Conference
IAM 2022
October 19-20, 2022, Lisbon, Portugal

IAM 2022-96740

A MULTI-MODAL DATA-DRIVEN DECISION FUSION METHOD FOR PROCESS MONITORING IN METAL POWDER BED FUSION ADDITIVE MANUFACTURING

Zhuo Yang[1,2], Jaehyuk Kim[1], Yan Lu[3, *], Ho Yeung[3], Brandon Lane[3], Albert Jones[3], Yande Ndiaye[1]

[1]Associate at National Institute of Standards and Technology, Gaithersburg, MD
[2]Georgetown University, Washington, DC
[2]National Institute of Standards and Technology, Gaithersburg, MD

ABSTRACT

Data fusion techniques aim to improve inference results or decision making by 'combining' multiple data sources. Additive manufacturing (AM) in-situ monitoring systems measure various physical phenomena and generate multiple types of data. Data types can occur at different scales and sampling rates during an AM build process. Data types that can be used to monitor the state of that process. Monitoring typically requires software tools to analyze data from multiple sources. There are two reasons. First, data only from one data source may not be accurate enough or large enough to monitor the process accurately. Second, a single source will be limited by the relevancy of the observations, signal-to-noise ratio, or other measurement uncertainties.

This work proposes a decision-level, multimodal, data fusion method that combines multiple, in-situ, AM monitoring data sources to improve that accuracy. The work is based on a recent, laser powder bed fusion (LPBF) experiment that was conducted at NIST to create overhang surfaces during a 3D part build. The data from that experiment is used to illustrate and validate the proposed method. The experiment involved using constant laser power and scan speed. The resulting overhang features were designed with different shapes. angles, and build locations.

A high-frequency, coaxial melt-pool, imaging system and a low-frequency layerwise staring camera are the two, in-situ, monitoring, data sources used in that experiment. The Naïve Bayes and the k-nearest-neighbor algorithms are first applied to each data set for overhang feature detection. Then both hard voting and soft voting are adopted in fusing the classification outcomes. The results show that while none of the individual classifiers are perfect in detecting overhang features, the fused decision of the 324 test samples achieved 100 % detection accuracy.

Keywords: Powder Bed Fusion, Additive Manufacturing, Decision Fusion, Data Fusion, Bayesian Network, Classification

1. INTRODUCTION

Additive Manufacturing (AM) technologies use powder materials to fabricate parts with complex geometries. Quality assurance is one of the biggest challenges for manufacturers to adopt those technologies [1]. The unique layer-by-layer building process expands the design options, freedoms, and spaces over traditional, subtractive processes [2]. However, in powder bed fusion (PBF) AM, this comes at increased costs. The costs are associated with the difficulty in controlling both the manufacturing process and the part quality. These difficulties emerge because parts undergo repeated and rapid melting and solidification. Our view is that we can improve AM part quality control using model-based, decision optimization.

Other researchers have held the same view. For example, one study shows a simple, decision-support model for choosing between additive and subtractive, to optimize energy efficiency [3]. Similar models may be applied when selecting the material and machine for a build. Often, these models result in feasible ranges for several, process parameters including 1) the required energy density per material melting temperature [4], 2) layer thickness per powder particle size [5] and 3) other dimensionless numbers [6]. While these ranges help choose process parameters for a given part, there is still no part-quality guarantee.

The authors' previous work involves analyzing, modeling, and optimizing a PBF process [7-9]. All three mostly rely on one process parameter, the current scan strategy, and one set of synchronized, in-situ, monitoring data [10-12]. Recently, more research efforts have been published that improve AM process controllability and part quality with in-situ monitoring data and advanced data analytics [13-16]. Data fusion is an advanced, data-analytics technique that integrates data from multiple sources. The fused data provides a comprehensive picture of the current process [17]; and it can be used to optimize decisions related to the future process parameters.

Figure 1 shows a multi-level, reference model for AM data fusion, which combines multiple streams of in-situ AM data to identify the state of a build process [18]. At the bottom level,

*yan.lu@nist.gov

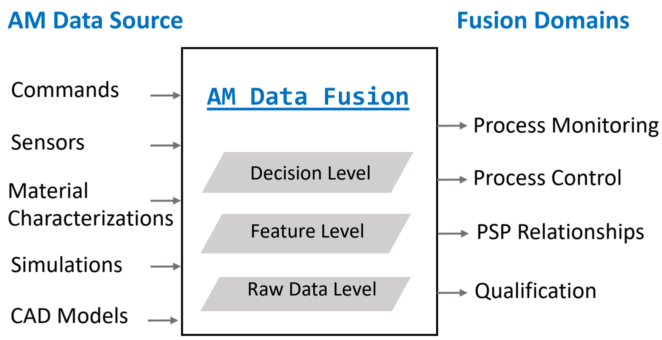

Figure 1. AM data fusion framework

fusion combines all raw data and creates an input file for decision making software. Such a file will have no information loss, but it will most likely suffer from data imbalance [19]. At the next level, data features provide the basis for the fusion model. For example, remelting maps reflect the current melting conditions of a layer by fusing melt-pool, image features with the scan commands. The fused data can be used to determine whether an overhang of the physical AM part is under or over fused [20].

The authors' previous work fused layerwise, build-surface images with high-frequency, coaxial, melt pool images. They then correlated those images to assess different geometric features such as overhangs [21]. However, the initial uncertainties in both data sources prevent building accurate point-to-point correlations. Moreover, it is difficult to build a data-driven model using features extracted from one dataset to predict features based on a different dataset.

The ability to make good decisions based on a single, data source may be limited due to the noise, algorithm, data characteristic, and data instance. However, such a single-source decision can avoid the accumulated uncertainty that results from feature-level fusion. On the other hand, a high initial noise of the source or misaligned data from that source can aggravate this situation. In addition, data from a single source may be sensitive to different processing conditions. For example, layerwise image (LWI) data can be good source for measuring surface texture though it has a lower resolution. Melt pool monitoring (MPM) images provide detailed melting conditions on a smaller scale but lack an overall representation of the entire layer.

While it is difficult to use ONLY one data source to make a good decision about the current AM process and parts, it is possible to integrate multiple, independent, data sources into a single, consolidated decision. We call this integration process decision fusion [22]. The final, fused decision is not limited by a fixed integration strategy because users can design relevant rules based on their preferences and expectations.

We believe that our proposed decision-fusion method, which is based on a hierarchical voting system, can make very accurate predictions. The foundation of the system derived from what we call individual classifiers. Section 2 will introduce the classification and voting methods. Section 3 presents the general workflow of the multi-modal, decision-fusion method for AM. Section 4 has details about the experimental design and basic data analysis. Section 5 demonstrates a case study using the proposed method to identify the overhang and non-overhang surface. The last section provides summary and future works.

2. BACKGROUND

The AM process-monitoring problem can be formulated as a classification task with input data $X = \{x_1, \dots, x_n\}$ at an index i ,classes of the process state represented as $Y \in \{y_1, \dots, y_m\}$ at an index j, and a classifier F which predicts Y from X; $F: X \to Y$

2.1 Classification methods

2.1.1 Naïve Bayes

Naive Bayes (NB) is a simple method that uses a probabilistic model for classification tasks [23]. Given $X = \{x_1, x_2, x_3, \dots, x_n\}$, a class probability $P(y_j|X)$ can be estimated with Bayes' theorem as like:

$$P(y_j|X) = \frac{P(x_1, x_2, x_3, \dots, x_n|y_j)P(y_j)}{P(X)} \tag{1}$$

$$P(X) = \sum_j^m P(x_i|y_j)P(y_j) \tag{2}$$

$P(y_j)$ and $P(x_i|y_j)$ can be easily estimated since they are the frequency of class y_j and each feature x_i for y_j in the training dataset respectively. For the joint probability $P(x_1, x_2, x_3, \dots, x_n|y_j)$, NB utilizes "native" assumption: the input feature x_i is independent of any other features. Then, the joint probability can be expressed as a product of each feature probability.

$$\begin{aligned} &P(x_1, x_2, x_3, \dots, x_n|y_j) \\ &= P(x_1|y_j)P(x_2|y_j)P(x_3|y_j) \cdots P(x_n|y_j) \\ &= \prod_i P(x_1|y_j) \end{aligned} \tag{3}$$

Therefore, the class with the highest probability is chosen as the predicted class $\hat{y}$.

$$\begin{aligned} \hat{y} &= \underset{j}{argmax}\ P(y_j|X) \\ &= \underset{j}{argmax} \frac{P(x_1, x_2, x_3, \dots, x_n|y_j)P(y_j)}{P(X)} \\ &= \underset{j}{argmax} \prod_i P(x_i|y_j)\,P(y_j) \end{aligned} \tag{4}$$

2.1.2 Deep feedforward Neural Network

A Deep Feedforward Neural Network (DFNN) uses a unidirectional (feedforward) information flow [24]. DFNN consists of three layers: an input layer that receives the input, an output layer that transmits the output, and a hidden layer that transforms the input into the latent representation. For the classification task, DFNN aims to learn a latent representation of a set of input X, which can be classified into different classes.

Our DFNN consists of L layers and that each layer l has M_l neurons at index n. $M_{l=1}$ for the input layer and $M_{l=N}$ for the output layer. L and M are determined by the dimension of X and the number of classes c for the classification task. $Y \in \mathbb{R}^m$ can expressed as a vector with dimension m. Then, an output z^l of each layer can expressed as like:

$$z^l = \sigma(w_n^T x_n^{l-1} + b_n)$$
$$for \;\; l = 1,2,\dots,L, \;\; n = 1,2,\dots,N_l \tag{5}$$

$$\underset{w_n, b_n}{\operatorname{argmin}} Loss(\, z^{i=N}\,, y\,) \tag{6}$$

where w_n^T and b_n are a weight and a bias of n^{th} neuron in l^{th} layer; x_n^{l-1} is an input of n^{th} neuron in $l - 1^{th}$ layer; σ is a nonlinear, activation function in which sigmoid and relu function are commonly utilized.

The optimal w_n^T and b_n are obtained by minimizing a $Loss$ function, which means difference between the final output $z^{i=N}$ and class vector y for each input X (Equ. 6). The optimization uses back propagation of the gradient of the $Loss$ function through the network.

For the classification task, a softmax function is used as the output layer's activation function. Softmax normalizes the output layer's vectors $w_n^T x_n^{l-1} + b_j,\; n = 1,2,\dots,M_{l=L}$ to values of the between 0 and 1, and the sum of the values is always 1. It allows $z^{l=L} \in \mathbb{R}^{M_{l=L}}$ to be interpreted as a class probability. The class with the highest probability is chosen as the predicted class label $\hat{y}$ based on the following

$$\hat{y} \;=\; \underset{j}{argmax}\; P(y_j|X) \tag{7}$$

2.1.3 k-Nearest Neighbor (kNN)

The k-Nearest Neighbor (kNN) is a distance-based classification method [25]. The kNN classifies new unlabeled data based on the majority vote of its k-nearest neighbors in the training set. When given the value of k, the k-nearest neighbors in that set are identified based on a distance metric. Then, the class probability can be expressed as the $Frequency_j$ of frequency of each class:

$$P(y_j|X) = \frac{Frequency_j}{k} \tag{8}$$

The class with the highest probability is chosen as the predicted class label $\hat{y}$, just like (7).

2.2 Voting Strategies

This section introduces three common voting strategies for deciding among the predictions of multiple classifiers.

2.2.1 Hard Voting

Hard voting is a simple method to select the best decision [4]. When the classifier $F_p(X)$ predicts a class probability, most votes ($mode$) of predicted classes from multiple classifiers is chosen.

$$F_p(X) \;=\; \underset{j}{argmax}\; P(y_j|X), for\; p = 1,2,\dots,P \tag{9}$$

$$\hat{y} = mode\{F_1(X), F_2(X), \dots, F_p(X)\} \tag{10}$$

2.2.2 Soft Voting

Soft voting is a weighted voting based on each class probability [26]. When given the class probability of each classifier $P_p(y_j|X)$ with classifier weight w_p, the most class probability from averaging the class probabilities of each classifier is chosen.

$$\hat{y} \;=\; \underset{j}{argmax} \sum_{p}^{P} w_p P_p(y_j|X) \tag{11}$$

$$w_p \;=\; \frac{1}{P} \tag{12}$$

2.2.3 Soft Voting with Entropy

Instead of using uniform weights (Equ. 12), soft voting can use weights that reflect the uncertainty about how confident the classifier is in its prediction. Here, entropy can be used to quantify the uncertainty [27]. When given the class probability of each classifier $P_p(y_j|X)$, classifier weight w_p is calculated to entropy and is normalized with Euclidean norm $||w||$

$$w_p \;=\; -\sum_{j=1}^{m} P_p(y_j|X)\log_2 P_p(y_j|X)\,, for\;\; p = 1,2,\dots,P \tag{13}$$

$$\overline{w}_p = \frac{w_p}{||w||} \tag{14}$$

3. A MULTI-MODAL, DATA-DRIVEN, DECISION FUSION METHOD FOR AM IN-SITU MONITORING

The proposed, data-driven, AM, decision fusion method includes two major parts. The first part generates an initial decision from individual classification models. The second part fuses those individual decisions using a new type of designed voting strategy, which is describe below.

Figure 2 shows an example of that strategy based on two, AM sensor systems with a total of 6 individual data sources. Each source collects different in-situ sensor data simultaneously during the AM build process. Each sensor can provide multiple datasets with multiple instances and characteristics. For example, an LWI camera can provide image data using different flash conditions, focus areas, and exposure times. During the PBF process, an LWI camera can capture details of the surface texture based on a specific light source and scan direction.

Unique features can be extracted from the same multi-characteristic dataset by using different processing methods. For example, one method can extract physical features of the melt-pool images based on thermal conditions and scanning behaviors. Another method can process the same images mathematically without any physical explanation. From even a single dataset, multi-algorithmic results can be derived using different classification methods.

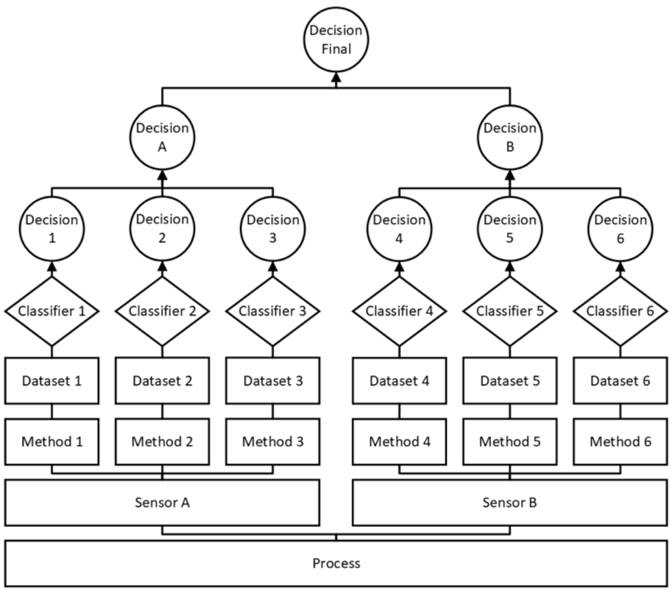

Figure 2. Workflow for a two-sensors example.

The six decisions from the six individual sensors will go through the voting system resulting in two decisions (Decision A and Decision B) fusion. After the two individual decisions have been made, they will be fused to create the Decision Final.

4. EXPERIMENTAL DESIGN AND BASIC DATA ANALYSIS

4.1 Experimental Platform

A 3D part was created on the Additive Manufacturing Metrology Testbed (AMMT) at the National Institute of Standards and Technology (NIST). AMMT is a fully customized metrology instrument that enables flexible control and measurement of Laser PBF processes [10, 11]. More details about AMMT can be found in Lane et al, 2020 [10].

4.2 Part Geometry

In this experiment, the 3D part was built on a wrought nickel alloy 625 (IN625) substrate - 100 mm x 100 mm x 12.5 mm. The part has a bounding box 5 mm x 9 mm x 5 mm, a 45-degree overhang feature, and a cylinder cavity. The powder material is a mix of recycled and virgin IN625 powder. The build consists of 250 layers at 20 µm per layer. The build employs a constant speed (800 mm/s), constant power (195 W), and a striped scan pattern [11]. The scan direction is designed to rotate 90 degrees after every layer. This study focuses only on the sensor data and not the process parameters that created that data.

Figure 3 shows the designed part, its dimensions, and its key geometric features. The part is 5 mm x 5 mm x 9 mm with 250 layers, where the layer thickness is 20 µm. The part has four regions. Zone-1 represents the regular region in the middle of the part. This is a 5 mm x 5 mm x 3 mm volume without overhang. Zone-2 is a 5 mm x 5 mm x 3mm volume on the far side with a fixed 45° overhang growth starting from Layer 52. The near side has a cylinder hole with 4 mm and 3 mm depth diameter.

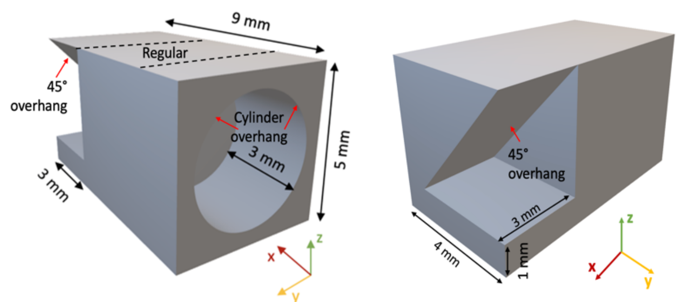

Figure 3. Part dimensions and key geometric features.

This part creates two, mirrored, overhang regions starting from Layer 126 and ending with Layer 225. Notes: Due to the cylinder's changing curvature, the overhang would change its size. Later layers would have a more intense overhang than earlier layers. Zone-3 and Zone-4 represent the overhang regions on this part. Figure 4 shows the top view (XY plane) of one mid-layer with all geometric features. It marks the details about the zone-division method.

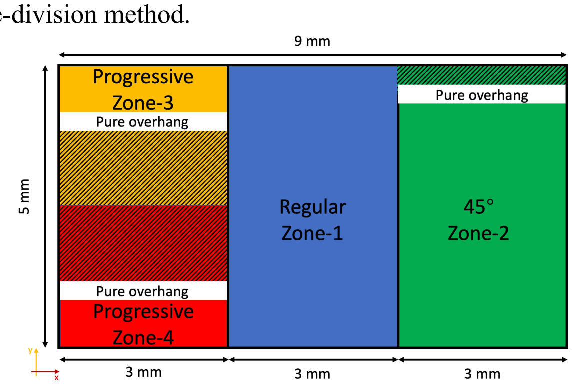

Figure 4. Zone division of the part form top view (XY plane).

4.3 Data Collection

This experiment collected two types of in-situ data, LWI images and MPM images. The experiment used three LED

*yan.lu@nist.gov

flashlights shooting from different angles, namely LED A, B, and C, in the building chamber for layerwise imaging. Once AMMT finished scanning one layer, the LWI camera captured one image under each flash condition. A high-speed, coaxial camera captured MPM images at a high frequency.

A preprocessing step deployed the 4-point homography method to correct the distortion and deformation of the raw LWI. Four corner points of the first layer with a rectangular cross-section were used to derive the homography matrix [28, 29]. Assuming that the distortion is identical for all the images - because the tower camera is stationary during the build process - the homography matrix is then applied to all the LWI images to align the pixels to the real-world coordinates.

Figure 5 shows the part surface of processed LWI images under three flash conditions. LWI data of LED A is not included in the case study due to over-exposure. As shown, the same surface from the same part exhibits different features. For example, LED B is sensitive to edge and powder. LED C is more sensitive to the surface texture.

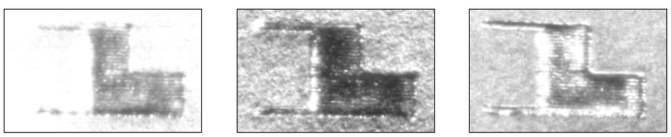

(a) (b) (c)

Figure 5. Part surface of three LWI images from three LED flashlight. (a) LED A, (b) LED B, (c) LED C.

Figure 6 shows three, sample, MPM images from the horizontal scan (a), the vertical scan (b), and the pre-contour scan (c), respectively. The white spot located at the image center is the laser melting area named melt pool. MPM images are measured 120 pixels by 120 pixels, where each pixel is 8 µm x 8 µm. The camera collects about 6000 MPM images at each layer. The exact number of images depends on the scanning time. More than 1.5 million MPM images were collected and used in this work.

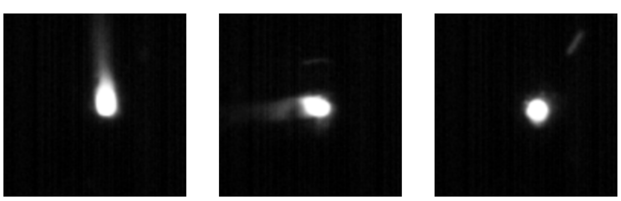

(a) (b) (c)

Figure 6. Sample MPM images at different moments.

4.4 Layerwise Feature extraction

This study focuses on two, layerwise, statistical features of each data source. MPM analysis studies the average, melt-pool size and its standard deviation per layer. LWI analysis focuses on the layerwise grayscale average value and standard deviation. The statistical features are extracted for the overhang and regular regions separately. Note, the numerical value from feature extraction is based on physical meanings. MPM feature directly represents the melt pool size behaviors, which affect by complex thermal conditions including energy input and heat conductivity. On the other hand, LWI features directly represent the surface texture and light sensitivity.

Figure 7 shows the LWI and melt pool size heat map of the same layer. The rectangular box marks the designed overhang region on this layer. The open system AMMT provide detailed digital command of laser position. Thus, this study has the ground truth of the overhang and non-overhang regions. The figures show the overhang region has higher grayscale and lower melt pool size.

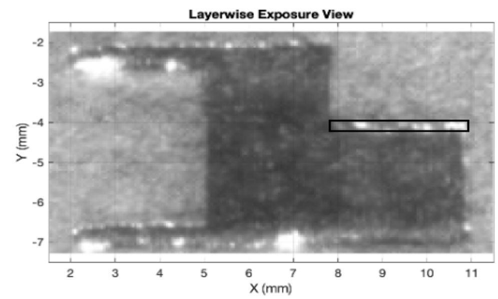

(a)

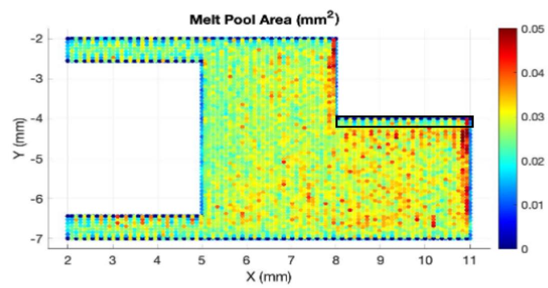

(b)

Figure 7. (a) LWI image for layer 151. (b) Calculated melt pool size heatmap of the same layer. Rectangular box marks the designed overhang region of the part.

To detect overhang features, only the melt pools and pixels on the edge of each layer would be included in the statistical analysis. That demands the feature extraction to precisely trim the data to the area with the strongest overhang effect. This study distinguished the pure overhang area based on the pixel size in the corrected LWI images. It analyzes the data from 1 to 4 pixels, where is 0.0649 to 0.2596 mm. Similarly, melt pools within this range are included to calculate the layerwise average and standard deviation for overhang and non-overhang regions.

4.5 Basic Feature Analysis

Figure 8 shows the average melt pool size from MPM and average grayscale value from LWI. The data exhibits clear difference between overhang (Zone-2 to 4) and non-overhang regions (Zone-1) in both data sources. Similarly, the standard deviation of melt pool size and grayscale value shows the same behavior.

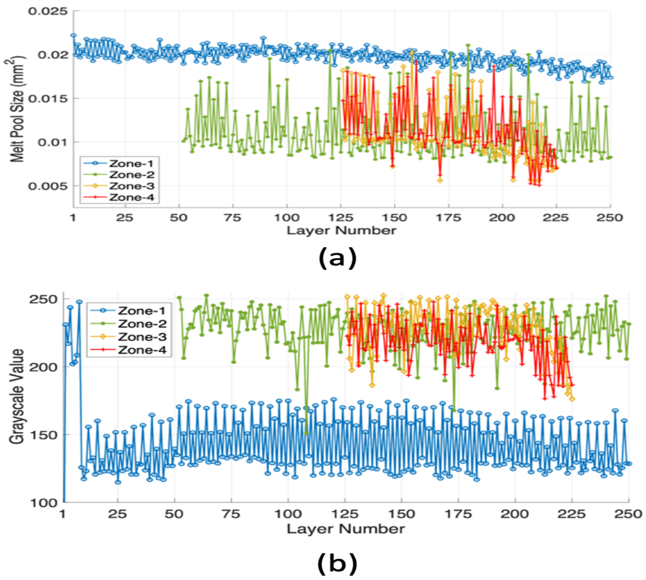

Figure 8. (a) Average melt pool size (b) Average grayscale value. Zone-1 is regular region without overhang. Zone-2 to 4 are 3 overhang regions with different degree.

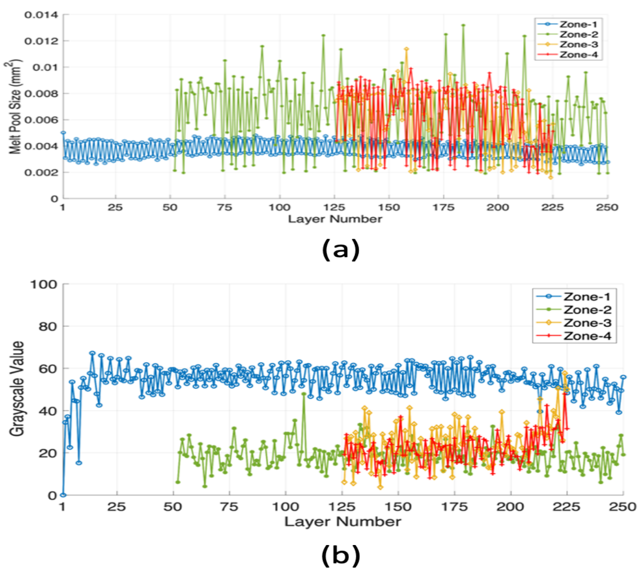

Figure 9. Standard deviation of melt pool size (a) standard deviation of LWI grayscale value (b).

As shown Figure 9, the non-overhang region is steadier than the overhang regions. According to this evidence, the case study selected the average and standard deviation as two input variables for the classification method. As a result, the following classification only selects the features that sensitive to overhang.

5. DEMONSTRATIVE CASE STUDY

Each dataset (see Figure 7) used in this study has 649 sample points. There are 250 non-overhang data points from Zone-1 (regular region). For overhang data, there are 199 data points from Zone-2 (45º overhang region) and 200 data points from Zone-3 and Zone 4 (cylinder hole overhang region). Zone-2, 3, 4 characterize the features based on the designed width of the overhang, in 1-4 pixel region. 1 pixel indicates the narrowest overhang region near the edge. 4 pixel indicates the overhang region has a wider range. As a result, each dataset of specific pixel width feeds into the individual classifier.

Figure 10 shows the prediction result of the three datasets in 1 pixel width. LED-B and LED-C deploy the NB method. MPM deploys the KNN method. Datasets LED B and LED C have two inputs: the average grayscale value and its standard deviation. Dataset MPM has two input variables: average, melt-pool size and its standard deviation. The data is evenly distributed, 50% training and 50% testing. All classifiers were created by Matlab 2022a classification functions, "fitcnb" for NB, "fitcnet" for DFNN, and "fitcknn" for KNN. Since the study focuses on decision fusion, the classifiers all deployed default settings without further modification.

The best algorithm for LED B is NB. The prediction accuracy is 97.84%, 97.22%, 96.60%, and 95.37% for pixel 1 to 4, respectively. KNN provides MPM with the best prediction results 100%, 100%, 99.69%, and 98.46%. None of the candidate algorithms could provide accurate predictions for LED C during the practice. In fact, the maximal, predictive accuracy is less than 80%. Due to the large difference to other sensorial datasets, later decision fusion would neglect the classifiers for LED C.

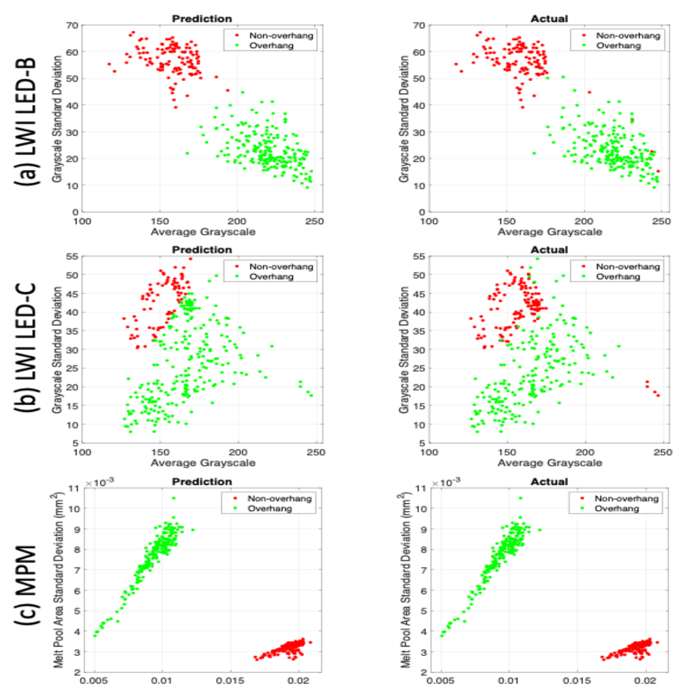

Figure 10. Prediction result for (a) LED-B with NB, (b) LED-C with NB, and (c) MPM with KNN.

Figure 11 shows the decision fusion result for Zone-3 at Layer 167 based on the individual decision of the 8 datasets of LED B and MPM. Datasets 1-4 represent the pixel 1-4 from sensor LED B. Datasets 5-8 are from MPM sensor. Orange color indicates the decision is overhang layer and green indicates non-overhang layer. The actual result is overhang.

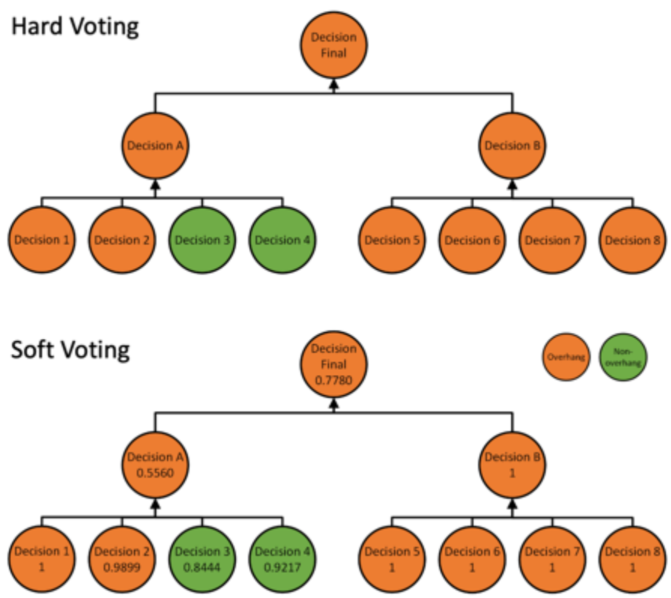

Figure 11. Decision fusion result based on hard voting and soft voting strategy.

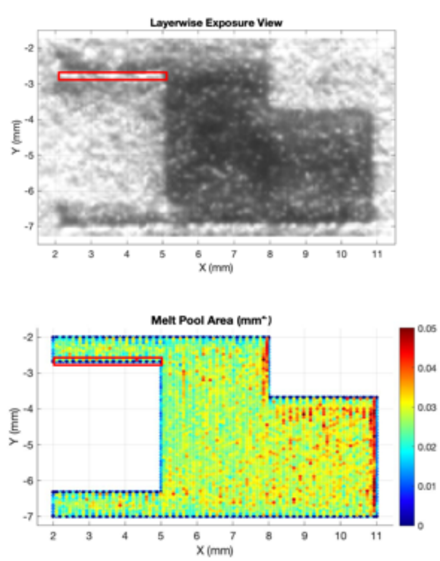

Figure 12. The actual LWI and melt pool size map of the same layer that mentioned in Figure 11. Red box marks the 4 pixels width overhang region at Zone-3 for LWI and MPM data.

Classifier 1-2 predict overhang, whereas Classifier 3-4 predict non-overhang. The fused decision of Sensor A is 50% for each. In this case, the rule determines overhang for equal voting to avoid false negative. Classifier 5-8 all predict overhang. According to the hard voting rules, the final decision is overhang. This solution agrees with the ground truth.

When using a soft voting strategy, the process relies on the probability of each prediction. Consequently, Sensor A has more than 50% voted for overhang when applying an equal weighting factor for each classifier. The final solution is the same as the hard voting strategy.

The decision fusion was based on a test computer with a is 2.9 GHz Quad-Core Intel Core i7 with 16 GB 2133 MHz LPDDR3 Ram. The incremental, computational cost of using decision fusion is negligible when compared to building individual models. Matlab 2021a uses averagely 0.2s to build individual model. Make decision from individual model for all test data is about 0.04s. Data fusion with soft voting strategy needs additional 0.1s.

6. SUMMARY AND DISCUSSION

This paper proposes a decision fusion method for AM. The method builds an individual data-driven model for each multi-modal data source. Each source will have its own characteristics, and instances. Then, our method makes an individual decision based on each model. Next, it fuses those individual decisions based on a voting system.

The case study focused on whether an overhang existed on an AM part. Overhang and non-overhang surfaces are pre-designed at the CAD model level. So, users have the pre-determined ground truth of every position. Since this designed truth might not actually be the truth, we conducted a preliminary experiment, collected six sensor datasets, and made an overhang prediction based on those datasets. The experiment yielded two results. First, multi-modal data sources can avoid the limitations associated with using a single dataset. Second, the final, fused decision/prediction reduced, by as much as 5%, the errors associated with the individual predictions. Predictions that were based on individual data sources. Overhang can significantly affect the geometric accuracy and surface roughness.

Since research is still at an early stage, more experiments will be conducted. Based on this experiment, the selected, input features may not be the optimal choices for identifying the surface features. Other statistical features may further improve the predictive accuracy. Furthermore, this study did not dive deeply into classification algorithms. Since the focus was decision making, we intentionally maintained the individual data-driven models at a simple default status. Future works will investigate the decision fusion at the algorithm level. This step may eliminate the bias of algorithm selection to improve the accuracy for more complex problems.

DISCLAIMER

Certain commercial systems are identified in this paper. Such identification does not imply recommendation or endorsement by NIST; nor does it imply that the products identified are necessarily the best available for the purpose. Further, any opinions, findings, conclusions, or recommendations expressed in this material are those of the authors and do not necessarily reflect the views of NIST or any other supporting U.S. government or corporate organizations.

ACKNOWLEDGEMENTS

This material is based upon work supported by the National Institute of Standards and Technology (NIST).

REFERENCES

[1] Frazier, W. E., “Metal Additive Manufacturing: A Review”, Journal of Materials Engineering and Performance volume 23, (2014): pages1917–1928
[2] Zhang, C., Chen, F., Huang, Z., Jia, M., Chen, G., Ye, Y., ... & Lavernia, E. J. (2019). Additive manufacturing of functionally graded materials: A review. Materials Science and Engineering: A, 764, 138209.
[3] Watson, J. K., and K. M. B. Taminger. "A decision-support model for selecting additive manufacturing versus subtractive manufacturing based on energy consumption." Journal of Cleaner Production 176 (2018): 1316-1322.
[4] de Leon Nope, G. V., L. I. Perez-Andrade, J. Corona-Castuera, D. G. Espinosa-Arbelaez, J. Muñoz-Saldaña, and J. M. Alvarado-Orozco. "Study of volumetric energy density limitations on the IN718 mesostructure and microstructure in laser powder bed fusion process." Journal of Manufacturing Processes 64 (2021): 1261-1272.
[5] Jacob, Gregor, Gregor Jacob, Christopher U. Brown, and Alkan Donmez. The influence of spreading metal powders with different particle size distributions on the powder bed density in laser-based powder bed fusion processes. Gaithersburg, MD: US Department of Commerce, National Institute of Standards and Technology, 2018.
[6] T. Mukherjee, V. Manvatkar, A. De, T. DebRoy, Dimensionless numbers in additive manufacturing, Journal of Applied Physics. 121 (2017) 064904.
[7] Yeung, Ho, Zhuo Yang, and L. Yan. "A meltpool prediction based scan strategy for powder bed fusion additive manufacturing." Additive Manufacturing 35 (2020): 101383.
[8] Yang, Zhuo, Yan Lu, Ho Yeung, and Sundar Krishnamurty. "From scan strategy to melt pool prediction: A neighboring-effect modeling method." Journal of Computing and Information Science in Engineering 20, no. 5 (2020): 051001.
[9] Yang, Zhuo, Yan Lu, Ho Yeung, and Sundar Kirshnamurty. "3d build melt pool predictive modeling for powder bed fusion additive manufacturing." In International Design Engineering Technical Conferences and Computers and Information in Engineering Conference, vol. 83983, p. V009T09A046. American Society of Mechanical Engineers, 2020.
[10] Lane, Brandon, Sergey Mekhontsev, Steven Grantham, M. L. Vlasea, Justin Whiting, Ho Yeung, Jason Fox et al. "Design, developments, and results from the NIST additive manufacturing metrology testbed (AMMT)." In 2016 International Solid Freeform Fabrication Symposium. University of Texas at Austin, 2016.
[11] Praniewicz, Max, Brandon Lane, Felix Kim, and Christopher Saldana. "X-ray Computed Tomography Data of Additive Manufacturing Metrology Testbed (AMMT) Parts:" Overhang Part X4"." Journal of Research of the National Institute of Standards and Technology 125 (2020): 1-9.
[12] Teixeira, Óscar, Francisco JG Silva, Luís P. Ferreira, and Eleonora Atzeni. "A review of heat treatments on improving the quality and residual stresses of the Ti–6Al–4V parts produced by additive manufacturing." Metals 10, no. 8 (2020): 1006.
[13] M. Grasso, A. Remani, A. Dickins, B.M. Colosimo, R.K. Leach, In-situ measurement and monitoring methods for metal powder bed fusion: an updated review, Meas. Sci. Technol. 32 (2021) 112001.
[14] R. McCann, M.A. Obeidi, C. Hughes, É. McCarthy, D.S. Egan, R.K. Vijayaraghavan, A.M. Joshi, V. Acinas Garzon, D.P. Dowling, P.J. McNally, D. Brabazon, In-situ sensing, process monitoring and machine control in Laser Powder Bed Fusion: A review, Additive Manufacturing. 45 (2021) 102058.
[15] S.S. Razvi, S. Feng, A. Narayanan, Y.-T.T. Lee, P. Witherell, A Review of Machine Learning Applications in Additive Manufacturing, in: American Society of Mechanical Engineers Digital Collection, 2019.
[16] L. Meng, B. McWilliams, W. Jarosinski, H.-Y. Park, Y.-G. Jung, J. Lee, J. Zhang, Machine Learning in Additive Manufacturing: A Review, JOM. 72 (2020) 2363–2377.
[17] Castanedo, Federico. "A review of data fusion techniques." The scientific world journal 2013 (2013).
[18] Yang, Zhuo, Yan Lu, Simin Li, Jennifer Li, Yande Ndiaye, Hui Yang, and Sundar Krishnamurty. "In-Process Data Fusion for Process Monitoring and Control of Metal Additive Manufacturing." In International Design Engineering Technical Conferences and Computers and Information in Engineering Conference, vol. 85376, p. V002T02A072. American Society of Mechanical Engineers, 2021.
[19] Rocío Ríos-Reina, Silvana M. Azcarate, José M. Camiña, Héctor C. Goicoechea, “Multi-level data fusion strategies for modeling three-way electrophoresis capillary and fluorescence arrays enhancing geographical and grape variety classification of wines”, Analytica Chimica Acta, Volume 1126, 2020, Pages 52-62, ISSN 0003-2670, https://doi.org/10.1016/j.aca.2020.06.014.
[20] Yang, Zhuo, Yan Lu, Brandon Lane, Jaehyuk Kim, Yande Ndiaye, and Sundar Krishnamruty. "Analyzing Remelting Conditions based on In-Situ Melt Pool Data Fusion for Overhang Building in Powder Bed Fusion Process." In 2021 International Solid Freeform Fabrication Symposium. University of Texas at Austin, 2021.
[21] Zhuo Yang, M. Adnan, Yan Lu, Fan-Tien Cheng, Haw-Ching Yang, Milica Perisic, Yande Ndiaye, Investigating Statistical Correlation Between Multi-Modality In-Situ Monitoring Data for Powder Bed Fusion Additive Manufacturing, IEEE CASE 2022 [under review]
[22] ISO/IEC TR 24722:2015, Information technology — Biometrics — Multimodal and other multibiometric fusion
[23] Berrar, Daniel. "Bayes’ theorem and naive Bayes classifier." Encyclopedia of Bioinformatics and Computational Biology: ABC of Bioinformatics 403 (2018).
[24] Svozil, Daniel, Vladimir Kvasnicka, and Jiri Pospichal. "Introduction to multi-layer feed-forward neural networks." Chemometrics and intelligent laboratory systems 39.1 (1997): 43-62.
[25] Sun, Shiliang, and Rongqing Huang. "An adaptive k-nearest neighbor algorithm." 2010 seventh international conference on fuzzy systems and knowledge discovery. Vol. 1. IEEE, 2010.
[26] Karlos, Stamatis, Georgios Kostopoulos, and Sotiris Kotsiantis. "A soft-voting ensemble-based co-training scheme using static selection for binary classification problems." Algorithms 13.1 (2020): 26.
[27] Namdari, Alireza, and Zhaojun Li. "A review of entropy measures for uncertainty quantification of stochastic

processes." Advances in Mechanical Engineering 11.6 (2019): 1687814019857350.

[28] Lu, Yan, Zhuo Yang, Jaehyuk Kim, Hyunbo Cho, and Ho Yeung. "Camera-based coaxial melt pool monitoring data registration for laser powder bed fusion additive manufacturing." In ASME International Mechanical Engineering Congress and Exposition, vol. 84492, p. V02BT02A045. American Society of Mechanical Engineers, 2020.

[29] Feng, Shaw, Yan Lu, Albert Jones, and Zhuo Yang. "Additive Manufacturing In-situ and Ex-Situ Geometric Data Registration." Journal of Computing and Information Science in Engineering (2022): 1-13.

